



## Validation of GOES-16 ABI and MSG SEVIRI active fire products

J.V. Hall<sup>a,\*</sup>, R. Zhang<sup>a</sup>, W. Schroeder<sup>b</sup>, C. Huang<sup>a</sup>, L. Giglio<sup>a</sup>

<sup>a</sup> University of Maryland, Department of Geographical Sciences, College Park, MD, USA

<sup>b</sup> NOAA/NESDIS/OSPO Satellite Analysis Branch, College Park, MD, USA

### ARTICLE INFO

**Keywords:**

Fire  
Biomass burning  
GOES ABI  
MSG SEVIRI  
Landsat

### ABSTRACT

The recent deployment of the next generation of geostationary weather satellites provides an opportunity for the establishment of a robust global network of geostationary fire data that can greatly complement existing polar-orbiting satellite fire products. Among other benefits, geostationary satellites provide frequent sampling of diurnal variations in fire activity. Building on established satellite active fire data validation protocols, we used Landsat-8 Operational Land Imager (OLI) as reference fire data to validate the fire products derived from two geostationary satellite sensors: the Advanced Baseline Imager (ABI) on board the National Oceanic and Atmospheric Administration (NOAA) GOES-16 satellite (launched November 2016), and the Spinning Enhanced Visible and Infra-Red Imager (SEVIRI), on board the European Organization for the Exploitation of Meteorological Satellites (EUMETSAT) Meteosat Second Generation (MSG) satellite series (multiple launch dates). The two primary algorithms associated with these geostationary active fire data sets are the Fire Detection and Characterization (FDC) product based on the heritage Wildfire Automated Biomass-Burning Algorithm (WF-ABBA) for the GOES-series, and the Fire Radiative Power (FRP-PIXEL) product based on the Fire Thermal Anomaly algorithm (FTA) for the MSG series. Our standardized validation method allowed for a direct inter-comparison between the complementary active fire datasets. Specifically, we present an error assessment of the detection probability (omission error) and false alarm rate (commission error) for two periods in 2017 and 2018 that include extensive fire activity in the respective full-disk sectors covered by each product. The results highlight (i) the restrictiveness of the FRP-PIXEL product (98% omission error) compared to the FDC product (84% omission error), and (ii) the elevated false alarm rate of FDC (88% commission error) compared to FRP-PIXEL (8% commission error). These validation results will be used to help support the development of a harmonized global multi-sensor active fire dataset to be integrated into the Global Wildfire Information System (GWIS).

### 1. Introduction

Routine wildfire monitoring at regional to global scales is crucial for understanding the role of this phenomenon in Earth system processes (Bowman et al., 2009; Cochrane, 2003) as well as the resulting impacts on ecosystems, biodiversity, and human health (Lohman et al., 2007). Satellite remote sensing has enabled regional to global scale fire detection from square-meters to sub-hectare spatial resolutions (e.g. Giglio et al., 2008, 2016; Justice et al., 2002; Picotte et al., 2016; Prins et al., 1998; Schroeder et al., 2016). The now widespread use of satellite-based active fire data sets for both research and operational (including near-real time) applications make validation of these data an essential element/prerequisite in understanding the differences, strengths, and limitations of these data, particularly when they are used (as is often the case) in combination. Geostationary satellites, in

particular, can provide repeated observations on a sub-hourly basis, making it possible to detect fires not detectable at longer temporal intervals (Schroeder et al., 2008a). Active fire products derived from geostationary sensors are consequently crucial inputs used in various operational hazard mapping systems (e.g., the National Oceanic and Atmospheric Administration [NOAA] Hazard Mapping System Fire and Smoke Product) which are often utilized by fire managers and first responders. It is therefore imperative to ensure these operational active fire products are reliable.

Of the various satellite based active fire products, those derived from the Moderate Resolution Imaging Spectroradiometer (MODIS) are perhaps the most widely used due to the long term, daily global coverage afforded by the Terra (launched 1999) and Aqua (launched 2002) satellites on which the two MODIS instruments reside. In comparison, the previous generation geostationary satellite-based active fire

\* Corresponding author.

E-mail address: [jhall1@umd.edu](mailto:jhall1@umd.edu) (J.V. Hall).

**Table 1**

Summary of the key advances in the latest generation of geostationary Earth observation satellites, compared to their predecessors.

Geostationary Sensor	Spatial Resolution* (km)	Spectral Bands	Mid-wave Infrared Channel Saturation (K)	Full-Disk Temporal Resolution (min)
Previous Generation GOES Imager	4	5	335	180
GOES-R ABI	2	16	400	5–15
Meteosat First Generation MVIRI	5	3	250	30
Meteosat Second Generation SEVIRI	3	12	335	5–15
Previous Generation Himawari-7 (MTSAT-2)	4	5	330	30
Advanced Himawari Imager-8	2	16	400	10

\* Applicable to mid-wave infrared channel used in active fire detection.

products had smaller user bases, likely due to their generally lower sensitivity arising from the larger pixel size and lower dynamic range as compared to MODIS (Hyer and Reid, 2009; Xu et al., 2010). However, the new generation of geostationary weather satellites, which include the Advanced Himawari Imager (AHI) series launched by the Japan Meteorological Agency (JMA), the Geostationary Operational Environmental Satellite (GOES)-R series from NOAA, and the Meteosat Second Generation (MSG) from the European Organization for the Exploitation of Meteorological Satellites (EUMETSAT), have greatly improved spatial, temporal, and radiometric fidelity, with a correspondingly improved capability for fire detection (Table 1).

Various operational fire products are being generated from these satellites using different algorithms. The Fire Detection and Characterization (FDC) product derived from the Advanced Baseline Imager (ABI) of GOES-R is based on the heritage Wildfire Automated Biomass-Burning Algorithm (WF-ABBA) (Schmidt et al., 2012), which was first developed in the early 1990s and made fully operational in the early 2000s (Justice et al., 2002; Prins et al., 1998; Prins and Menzel, 1992). The Fire Radiative Power (FRP-PIXEL) active fire product from the MSG Spinning Enhanced Visible and Infra-Red Imager (SEVIRI) is produced using the Fire Thermal Anomaly (FTA) algorithm, which adopted the fundamentals from the MODIS active fire algorithm but was transformed and applied to the MSG SEVIRI sensor characteristics (Wooster et al., 2015). The FDC and the FRP-PIXEL products complement each other geographically, with the former providing optimum coverage over North, Central, and South America and the latter over Africa and much of Europe. However, because they are produced using different algorithms applied to observations acquired with different sensor characteristics, it is unlikely that their information content and uncertainty levels are comparable. Comprehensive assessments of both products using identical methods are needed to establish to what degree these products complement each other in terms of data quality and information content, and to determine if and how these products can be used together in global studies and/or to produce a harmonized active fire product suite. Despite our efforts to include other new generation geostationary data sets to provide a more complete global coverage (e.g., JMA's Advanced Himawari Imager, MSG SEVIRI located over the Indian Ocean, GOES-17 ABI), those complementary fire products were deemed non-operational ("beta" status) or inaccessible at the time of writing.

Here we provide an assessment of the FDC and the FRP-PIXEL products, building upon previous validation efforts that employed reference data derived from 20- to 30-m resolution Advanced Spaceborne Thermal Emission and Reflection Radiometer (ASTER) and Landsat imagery to validate contemporaneous 1-km Terra MODIS and 4-km GOES-12 Imager active fire products (Schroeder et al., 2008b, c). Our goal was to quantify the commission and omission errors of the two products during two periods in 2017 and 2018 that include extensive fire activity in the respective full-disk sectors covered by each product using near simultaneous Landsat-8 observations (i.e., within 5-minutes of the GOES-16 overpass and 6-minutes of the MSG overpass – see section 3) that were not obscured by clouds/shadow. We describe first the data and details of the FDC and FTA algorithms, followed by the methods used, followed in turn by our validation results and a final discussion.

## 2. Data

### 2.1. GOES-16 ABI

The GOES-16 satellite was launched in November 2016, becoming the first of the new GOES-R ABI series to enter operations. The satellite was positioned in a geostationary orbit over 75.2 °W, thereby occupying the "East" orbit of the two-satellite constellation of the operational GOES observing system. The "West" orbit (137.2 °W) has been recently occupied by the follow-on GOES-17 satellite launched in March 2018 – the corresponding fire product was still in beta status and not available to the public at the time of writing. GOES-16 ABI provides a vantage observational point of much of the Americas, in addition to oblique views of the western tip of Africa (Fig. 1).

Full-disk FDC fire data (Schmidt et al., 2012) were obtained from the NOAA Comprehensive Large Array-Data Stewardship System (CLASS) for the period 18 July 2018 – 30 September 2018 (75 days), which coincides with the peak fire activity (July/August) in the Americas. Although the ABI sensor has a 2-km pixel footprint at the subsatellite point, the area of this footprint systematically grows to more than 8 times larger with increasing view zenith angle. The FDC product is available every 5–15 minutes for the full disk sector, every 5-minutes for the Conterminous U.S. (CONUS) sector, and every 30–60 seconds for the mesoscale sector (variations in temporal frequency are based on scan mode used). For this study, we used the 15-minute full disk data which was available for the entire sampling period analyzed. Full disk and CONUS sectors experience the same data processing flow, therefore, full disk results are expected to be representative of CONUS data for similar observations. The FDC algorithm processing using high-frequency mesoscale data is not currently performed during regular operations. In total, 8352 full disk files were queried during the sampling period, of which 535 files were found to be near-coincident with Landsat imagery and therefore used in the validation analysis.

The FDC product contains information on the fire pixel locations, sub-pixel fire characteristics including active fire area and temperature, and fire radiative power (FRP), in addition to various data attributes including the start- and end-scan times. For each fire pixel detected, a corresponding class is assigned indicating the level of confidence as a function of processing conditions, as follows: 10 or 30 = processed fire pixel (highest confidence); 11 or 31 = saturated fire pixel; 12 or 32 = cloud contaminated fire pixel; 13 or 33 = high probability fire pixel; 14 or 34 = medium probability fire pixel; and 15 or 35 = low probability fire pixel. The class definitions above were derived from the Algorithm's Theoretical Basis Document (Schmidt et al., 2012) and generally describe the observation conditions encountered during analysis, gradually progressing from straightforward detection scenarios (class 10/30 involving well-defined fire and background pixel signatures) to more complex and/or ambiguous cases (class 15/35 involving relatively weak fire signature and/or poorly-characterized background). Class values 30–35 represent temporally filtered fire pixels, for which two collocated detections must be observed in less than 12-hs, thereby corresponding to a more conservative data subset as compared to class values 10–15 (Schmidt et al., 2012).

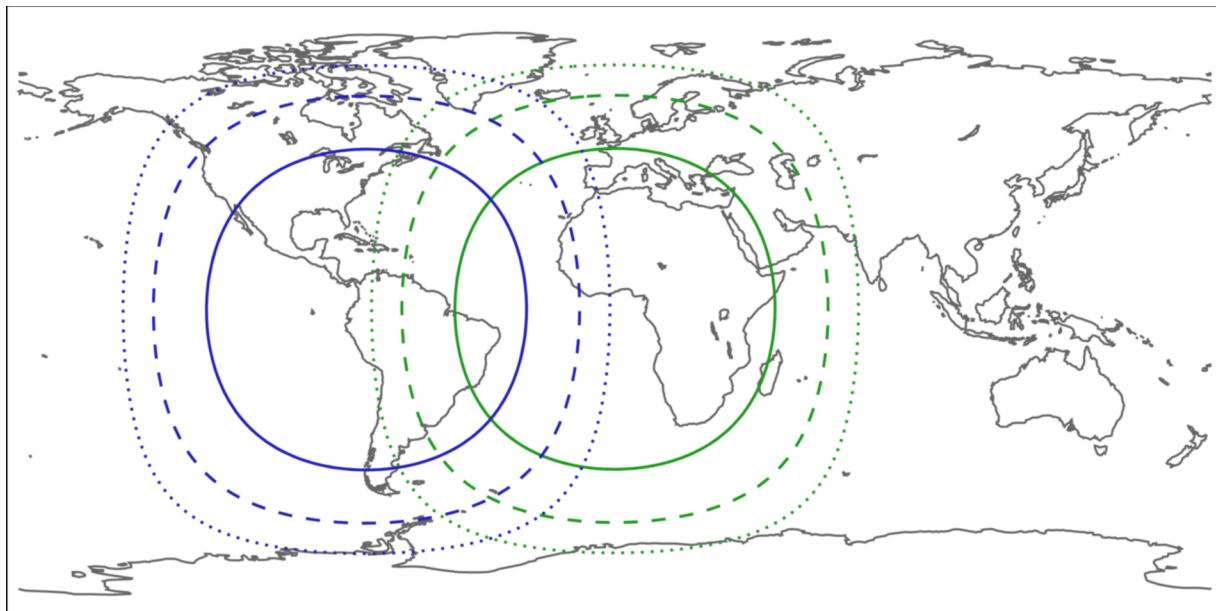


**Fig. 1.** Spatial coverage of geostationary fire data from the MSG SEVIRI (dark green outline) and GOES-16 ABI (blue outline) sensors used in this study. Solid, dashed, dotted lines indicate the boundaries at which the area of the pixel footprint grows to a factor of 2, 4, and 8 times larger than at the sub-satellite point. (For interpretation of the references to colour in this figure legend, the reader is referred to the web version of this article).

### 2.1.1. FDC algorithm

The current FDC algorithm is a “dynamic, multispectral thresholding, contextual algorithm” designed to identify fire pixels through a decision-tree approach comparing them with their neighboring non-fire background pixels (Schmidt et al., 2012). To retain cohesion between the older and newer generation GOES series satellite products, the current GOES-16 ABI FDC algorithm design draws heavily on the heritage GOES WF-ABBA thus ensuring continuity of the long-term geostationary active fire data record; however, with the improved spatial resolution of the GOES-R series, the minimum detectable fire size has decreased to approximately  $0.004 \text{ km}^2$  at the sub-satellite point (clear sky conditions, burning at 800 K). Despite the increase in spectral coverage from 5 channels (GOES Imager) to 16 channels (GOES ABI), the FDC algorithm still utilizes only 3 channels. Channels 7 (3.9  $\mu\text{m}$ ) and 14 (11.2  $\mu\text{m}$ ) data are used to locate and characterize the sub-pixel day and nighttime fire activity, in addition to daytime channel 2 (0.64  $\mu\text{m}$ ) data which is used to assist with cloud masking while also establishing the surface albedo value to help reduce the solar contamination effects in channel 7 (3.9  $\mu\text{m}$ ). Channel 15 (12.3  $\mu\text{m}$ ) is also used, but not required, to identify opaque clouds. One major improvement from the previous GOES Imager is the increased dynamic range of the GOES-R ABI channel 7, which allows a maximum sensing temperature of 400 K. This increased dynamic range covers a wide range of features from very cold convective cloud tops to very hot fires. According to Schmidt et al. (2012) and Koltunov et al. (2012), the elevated saturation temperature in channel 7 should reduce the number of saturated pixels (class 11 and 31) to less than 5% of all observed fires.

Alongside the calibrated ABI radiances and brightness temperatures (BT) acquired from the aforementioned spectral bands, the FDC algorithm also ingests a variety of dynamic and stationary ancillary data, including but not limited to: National Centers for Environmental Prediction Total Precipitable Water (TPW) (6-hs, 0.25°); TPW offset look-up table to adjust band radiances; MODIS global emissivity (monthly, 0.05°); and a variety of 1-km MODIS land cover products. All ancillary data are remapped to the ABI scan grid using a nearest-neighbor approach. Furthermore, the algorithm ingests the previously generated fire masks used in the temporal filtering, a process required for the assignment of ABI classes 30–35 in the final product output. In

addition, ABI sensor quality flags from the Level 1B data and the solar-view geometry data are also ingested since all fire processing is limited to satellite viewing angles less than 80°, with best results expected within 65° (see Schmidt et al., 2012 for more details on the algorithm input data).

The FDC algorithm uses a two-step approach. The first step (Part 1) is designed to identify all potential fire pixels while the second step (Part 2) further confirms and then characterizes the sub-pixel fire activity. A primary component of the Part 1 algorithm is referred to as “Reflectivity Product” in Schmidt et al. (2012) and is an approximation of the 3.9  $\mu\text{m}$  reflectance derived in conjunction with the 11.2  $\mu\text{m}$  BT. Using this reflectance layer, the primary loop moves through all pixels while various threshold tests are employed to create block-out zones (i.e. pixels are assigned specific fill values and masked from further analysis). These block-out zone tests search for (i) view zenith angles (VZA) less than 10° (as part of the sun glint test) or greater than 80°, (ii) sun glint angles less than 10°, (iii) non-fire ecosystems (e.g. water, deserts, coastlines) and, (iv) bad pixels – i.e. those pixels with a channel 7 or channel 14 BT above 5 K over the corresponding system-defined saturation temperature or those with a BT equal to the system-defined missing value.

A data quality check is performed once the block-out zones have been identified. Before several tests are performed to identify opaque clouds, cloud edges, and saturated pixels, minimum thresholds are set dynamically depending on the time of day with a maximum at noon. In addition, the 3.9  $\mu\text{m}$ –11.2  $\mu\text{m}$  difference output is tested against a minimum threshold of 2 K, and any pixels below this threshold are assigned a mask code and removed from further testing. After the initial quality check and the cloud, cloud edge, and saturated pixels tests have been performed, the algorithm determines the background statistics of the remaining valid land pixels using a dynamic window. This window expands (maximum 201 × 201 pixels) until at least 20% of the window contains cloud-free, non-hotspot pixels. Warm and cold pixel thresholds screen out anomalous hotspots and clouds from being included in the calculation of the background statistics. Various statistical test outputs are compared to determine the mean and standard deviation BT thresholds for the background pixels.

Another fundamental step within Part 1 of the algorithm is the determination of contextual thresholds within the background

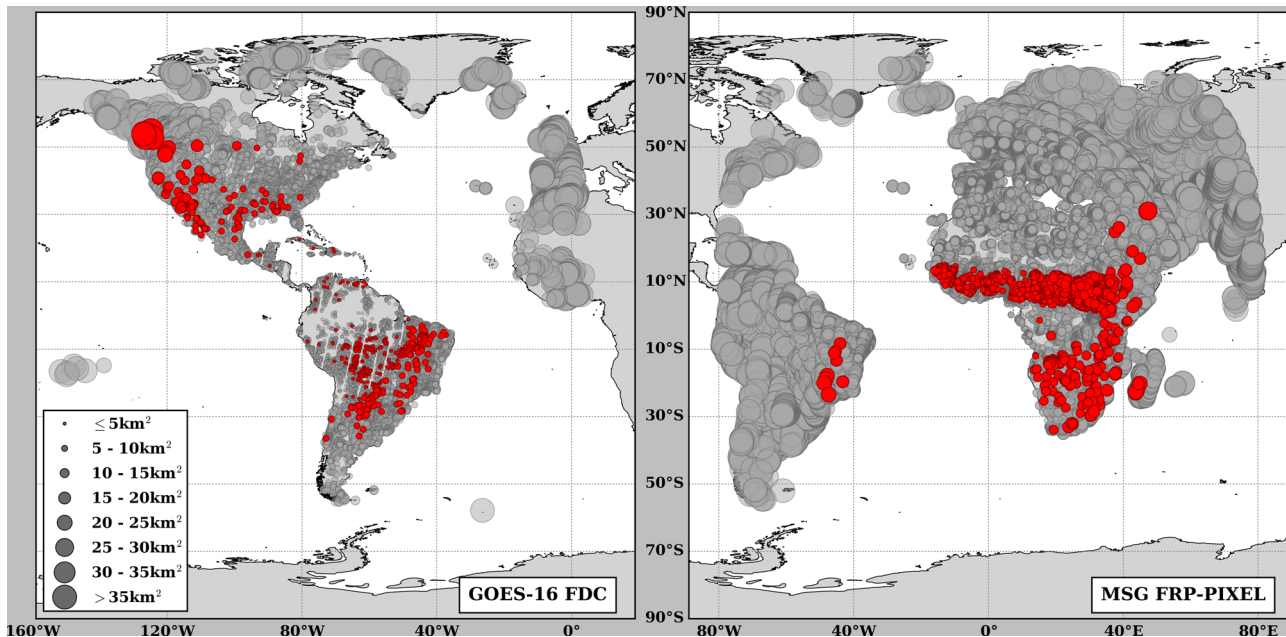


**Fig. 2.** GOES-16 FDC (left) and MSG FRP-PIXEL (right) validation points (grey circles represent pixel area in  $\text{km}^2$ ). To reduce clutter, only the highest probability FDC fire classes (10, 11, 30, and 31) are shown (red circles). Similarly, only FRP-PIXEL validation pixels with a confidence value over 50% are shown. (For interpretation of the references to colour in this figure legend, the reader is referred to the web version of this article).

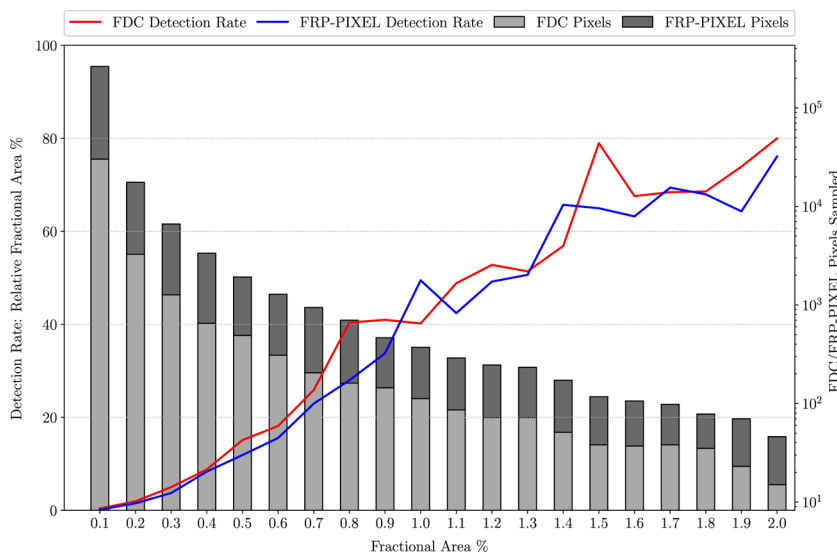


**Fig. 3.** Detection rates for FDC (red line), and FRP-PIXEL (blue line) active fire products as a function of relative fractional area. It was assumed the individual Landsat-8 OLI reference fire pixels corresponded to a 900-m<sup>2</sup> fire area. (For interpretation of the references to colour in this figure legend, the reader is referred to the web version of this article).

window. These thresholds are computed from the 3.9  $\mu\text{m}$  BT, 11.2  $\mu\text{m}$  BT, the 3.9  $\mu\text{m}$ –11.2  $\mu\text{m}$  BT, the 3.9  $\mu\text{m}$  reflectance, and the channel 2 (0.64  $\mu\text{m}$ ) albedo. These threshold tests (see section 3.4.2.6 in Schmidt et al., 2012) are fundamental for reducing false alarms caused by variations in channel BTs due to solar contamination, surface changes, or noise. These thresholds are applied to all potential fire pixels to further filter (or mask accordingly) non-fire pixels. For all remaining potential fire pixels, transmittance, emissivity, solar reflectivity, and diffraction corrections are applied to the observed 3.9  $\mu\text{m}$  and 11.2  $\mu\text{m}$  BT inputs. The NCEP TPW values from the ancillary look-up table are used to correct for water vapor. An additional correction, based on a heritage WF-ABBA regression analysis, is applied to BTs over transparent cloud/smoke-covered fire pixels for minimum attenuation situations only. A further correction for surface emissivity is carried out on the TPW-corrected radiance to increase the accuracy of the background and observed pixels actual emitting radiance. Finally, corrections are made for solar reflectivity and diffraction and the final corrected radiances

are converted back to channel temperatures using the Planck function.

Next, several post-correction tests are undertaken to characterize the sub-pixel characteristics and to finalize the identified fire pixels before the algorithm moves into Part 2. The first characterization test aims to estimate the instantaneous sub-pixel fire size and temperature using a modified bi-spectral retrieval (Dozier, 1981; Prins and Menzel, 1992, 1994). A fire pixel can only be classified as a “processed” fire in the final output if the iterative retrieval solution is within  $10^{-20}$  (radiance units) of the 3.9  $\mu\text{m}$  and 11.2  $\mu\text{m}$  adjusted radiances (see Table 3.7 and 3.8 in Schmidt et al., 2012 for equations and further details). Meanwhile, FRP is quantified based on a single-band (3.9  $\mu\text{m}$ ) middle infrared (MIR) radiance methodology (Wooster et al., 2003), which incorporates the pixel area, Planck’s Radiation Law, Stephan-Boltzmann Law, and the observed 3.9  $\mu\text{m}$  fire pixel and background radiances (see equation 3.4 in Schmidt et al., 2012). The current version of the algorithm computes FRP only for pixels that are not flagged as cloudy or saturated, therefore, all fires classed as ABI class 11, 12, or 15

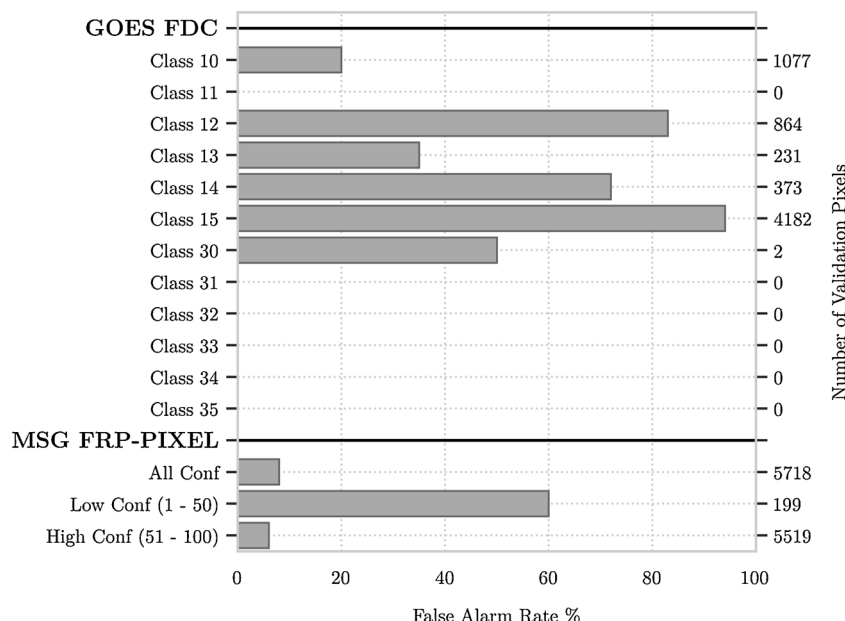


**Fig. 4.** FDC and FRP-PIXEL commission error. FDC classes: 10 or 30 = processed fire pixel (highest confidence); 11 or 31 = saturated fire pixel; 12 or 32 = cloud contaminated fire pixel; 13 or 33 = high probability fire pixel; 14 or 34 = medium probability fire pixel; and 15 or 35 = low probability fire pixel.

have no reported FRP value – future FDC versions are expected to include FRP retrievals for all fire pixel classes. Once all potential fire pixels are identified, an output is created to be fed into Part 2 of the algorithm. The output includes a unique identifier for all potential fire pixels along with a suite of complementary information (e.g., longitude, latitude, emissivity values, brightness temperatures, etc.).

Part 2 of the algorithm is designed to (i) further eliminate false alarms, (ii) determine the fire category, and (iii) apply temporal filtering before outputting the final FDC fire product. Additional threshold tests are performed to further eliminate any false alarms. During these tests, the algorithm also runs additional screenings for sun glint and reevaluates flagged fire pixels (from Part 1) along cloud edges. These threshold tests utilize values extracted from the surface albedo, solar zenith angle, 3.9  $\mu\text{m}$  BT, and various test outputs from Part 1 of the algorithm (see section 3.4.2.13 in Schmidt et al., 2012). All remaining fire pixels are then assigned categories (mask codes 10–15 and 30–35) based on information from Part 1 and Part 2 threshold tests. Codes 10–15 have not passed the temporal filtering screening, while codes 30–35 have passed the screening. Throughout the algorithm, various flags are assigned to a pixel depending on the outcome of the various tests. These flags are used to help determine the final fire category.

Finally, temporal filtering is applied to the Part 2 output before the creation of the final FDC output. The temporal filtering feature was designed to provide the user with a conservative fire product by exploiting the high temporal resolution of GOES-16. The algorithm is designed to track all previous fires from the past 12-hs and compares this mask to the current fire pixels. If a previous fire pixel was detected within 12-hs and within 1 pixel of the current fire pixel coordinates, the current fire pixel is given a temporally filtered mask code (30–35).

## 2.2. MSG SEVIRI

The SEVIRI full disk is centered at 0° and covers the African and European continents and portions of the eastern edge of South America (Fig. 1). At present, there are four MSG satellites in orbit; Meteosat-8 (launched 2002), Meteosat-9 (launched 2005), Meteosat-10 (launched 2012), and Meteosat-11 (launched 2015). The latest Meteosat-11 satellite replaced Meteosat-10 at 0° on 20 February 2018, becoming the primary operational MSG satellite and observing the full disk every 15-minutes, while the Meteosat-10 satellite now provides the Rapid

Scanning Service, delivering imagery over portions of Europe and Africa every 5-minutes. The FRP-PIXEL product (Wooster et al., 2015) was obtained from the EUMETSAT Satellite Application Facility on Land Surface Analysis (Level 2 LSA SAF; <https://landsaf.ipma.pt/en/>) (Trigo et al., 2011) for the period 1 November 2017 – 28 February 2018 (120 days), which coincides with the peak African burning period (December/January). The SEVIRI full disk scan moves from south-to-north and covers a period of 12.5-minutes, with a nominal refresh rate of 15-minutes (Aminou, 2002). Spatially, the SEVIRI fire product is slightly coarser than the ABI product, with a 3-km pixel footprint at the sub-satellite point. The FRP-PIXEL product is comprised of two separate files: (i) a List Product file containing the location and times of all active fire pixels detected, including a number of variables derived for each active fire pixel such as fire confidence (0–100%), FRP, and pixel area and (ii) a Quality Product file that contains detailed information on the processing status of each SEVIRI pixel. A total of 11,520 full disk files were queried during the sampling period, of which 1203 files were coincident with Landsat imagery and therefore used in the validation analyses.

### 2.2.1. FTA algorithm

EUMETSAT LSA SAF contains four near real-time and two reprocessed fire products: Fire Detection and Monitoring (LSA-501); Fire Radiative Power (LSA-502 – used in this study); Fire Radiative Power – Gridded (LSA-503); Fire Risk Map (LSA-504); Fire Radiative Power Reprocessed (LSA-550); and Fire Radiative Power – Gridded Reprocessed (LSA-551) (<https://landsaf.ipma.pt/en/products/fire-products/>). The FTA algorithm is used to deliver the four FRP products: LSA-501; LSA-502; LSA-550; and LSA-551, following a similar overall processing structure to the ABI FDC algorithm. Both algorithms are dynamic, rely on multispectral thresholding, and derive radiance and brightness-temperature statistics from non-fire background pixels. Both algorithms are also designed to first identify potential fire pixels and then confirm them on the second pass (or Part 2 for FDC) of the algorithm. Unlike FDC, the FTA algorithm was to some extent built on the well-established MODIS active fire algorithm and adapted to the MSG SEVIRI sensor characteristics (Giglio et al., 2003; Govaerts et al., 2016).

Overall, the FTA algorithm methodological framework contains several processing steps: (i) clear sky pixel identification, (ii) potential

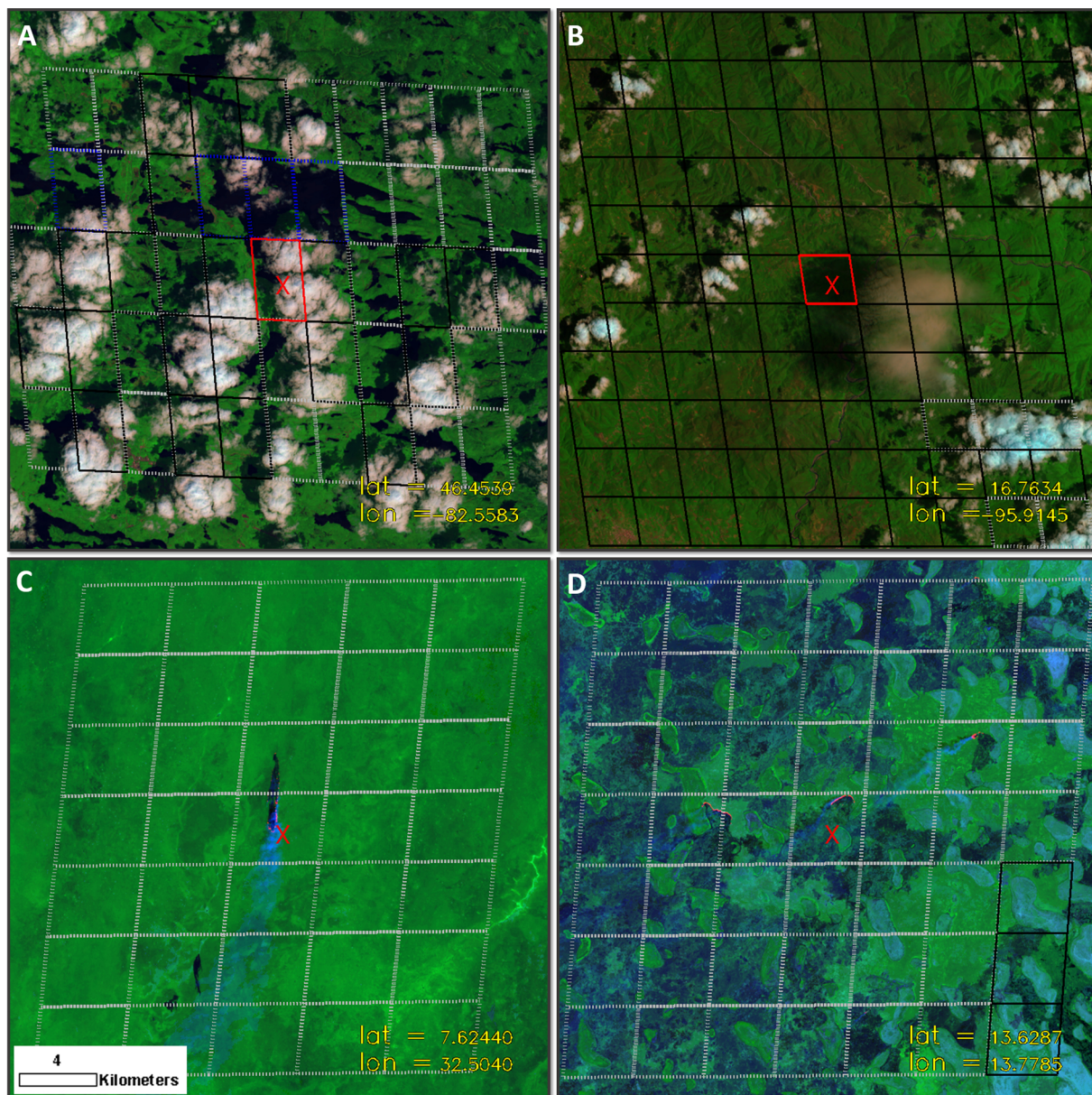


**Fig. 5.** Visual examples of the impacts from clouds/cloud-shadows in A and B (ABI), and an overzealous cloud mask in C and D (SEVIRI). White squares represent pixels identified as clouds, red squares represent pixels identified as a fire, and black represent pixels identified as clear land. The latitude and longitude values (bottom right in each panel) describe the approximate coordinate of the center of each pixel marked with a red 'X'. (For interpretation of the references to colour in this figure legend, the reader is referred to the web version of this article).

fire pixel identification, (iii) background pixel identification, (iv) FRP assessment, (v) FRP uncertainty estimation, and (vi) quality flag estimation (Govaerts et al., 2016; Wooster et al., 2015). The FTA algorithm relies on input from the Level 1.5 SEVIRI observed BT data and several ancillary datasets, including, the 1-km Global Land Cover (GLC 2000) to mask large water bodies, and the Nowcasting and Very Short Range Forecasting SAF (NWC SAF) cloud mask to remove cloud-contaminated pixels, both helping remove false alarms from specular reflections. According to Wooster et al. (2015), the FTA algorithm derives the cloud mask using the methods detailed in Derrien and Le Gléau, 2005 and MeteoFrance, 2007. During the development of the FTA algorithm, the developers found that active fires located under optically thin (e.g., Cirrus) clouds did not produce a thermal signature with sufficient contrast to the background, and therefore opted to mask out all cloudy pixels prior to detection of active fires (Wooster et al., 2015).

After the masking of water and cloudy pixels, the algorithm

identifies all potential fire pixels by applying a number of liberal spectral thresholds to the day and night  $3.9\text{ }\mu\text{m}$  BT and the  $(3.9\text{ }\mu\text{m} - 10.8\text{ }\mu\text{m})$  BT difference inputs (see Wooster et al., 2015 for details). The first stage of low sensitivity thresholds was designed to capture more potential fire pixels since the initial algorithm design led to too many missed active fires when compared to MODIS (Govaerts et al., 2016). However, these liberal thresholds also allow large swaths of homogeneously warm areas to be identified as fires. To reduce these false alarms, several high-pass filters and ratio tests are applied to the potential fire pixels to remove those affected by sun glint and to remove the large swaths of "fire" pixels in homogenously warm areas. The next stage is to compute the background pixel statistics using an expanding window (initial size:  $5 \times 5$  pixels; maximum size:  $15 \times 15$  pixels) until sufficient background pixels (65%) meet the various criteria outlined in Roberts et al. (2005) and Wooster et al. (2015). One important distinction is the FTA algorithm removes the immediate neighboring pixels

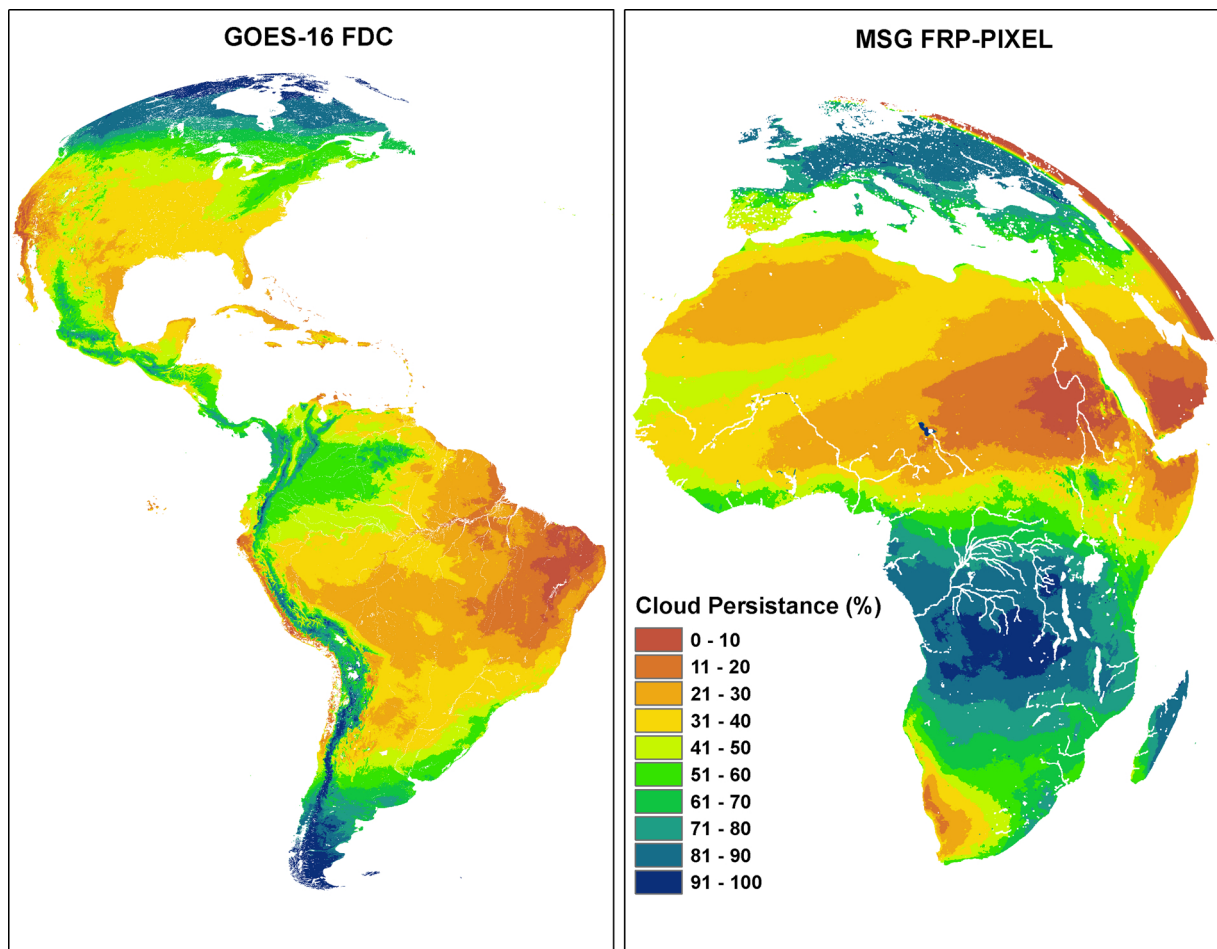


**Fig. 6.** FDC-derived cloud cover persistence (%) between 18 July 2018 and 30 September 2018 (left) and FTA-derived cloud cover persistence (%) between 1 November 2017 and 28 February 2018 (right). For display purposes, the tip of Western Africa (ABI) and the eastern edge of South America (SEVIRI) were removed from the full disk view.

from the background window calculations to reduce the impact of the point spread function.

Several statistical tests (detailed in [Roberts et al., 2005](#)) are applied to the potential fire pixel and the background pixels to determine the final classification of the fire pixels in the Quality Product (class 1 = confirmed active fire and FRP is estimated; class 2 = confirmed saturated active fire and FRP is estimated with adjustments) and the fire confidence (0–1) based on the approach by [Giglio et al. \(2003\)](#). As with the ABI algorithm, the FRP for both classes are also estimated using the MIR radiance approach ([Wooster et al., 2003](#)) and various quality flags are assigned throughout the algorithm's processing steps ([Wooster et al., 2015](#) Table S1).

### 2.3. Landsat-8 reference fire data

Reference fire data were derived from Landsat-8 Operational Land Imager (OLI) 30-m imagery using the [Schroeder et al. \(2016\)](#) Landsat-8 OLI automated fire detection algorithm. In total 19,979 Landsat-8 images were processed for this study. Each of these OLI reference images was visually inspected to ensure the quality of the OLI reference data removing, when necessary, reference masks that contained (i) artifacts from the original OLI input data and/or (ii) incorrectly mapped active fire pixels. These problems were mainly found in the mountainous regions at the northern edges of the MSG disk or in portions of western Africa and the Sahara Desert. In total, 186 (less than 1%) OLI reference files were removed as a result of the quality control check. Consequently, 5760 quality checked images were found coincident with

the ABI data, while 14,032 images matched the SEVIRI data.

### 2.4. Vegetation continuous fields and MODIS land cover data

Each ABI and SEVIRI validation pixel was assigned an average tree cover percentage and a majority land cover classification to help determine the impact of land cover on omission and commission errors. The percentage tree cover data, defined as the percent of a grid cell covered by tree canopy, was extracted from the 2017 500-m Moderate Resolution Imaging Spectroradiometer (MODIS) Vegetation Continuous Fields (VCF) Collection 6 data layer ([DiMiceli et al., 2011](#); [Hansen et al., 2002](#)). Average percentage tree cover estimates were calculated for a 20 × 20-km area centered on the corresponding ABI or SEVIRI pixel location for use in the validation analyses.

To simplify the land cover analysis, we aggregated the 17 distinct International Geosphere-Biosphere Programme (IGBP) land cover classes present in the MODIS Land Cover Type Collection 6 product (MCD12Q1, [Friedl and Sulla-Menashe, 2019](#)) for 2017 into 8 broader classes (forest, shrubland, savanna, grassland, cropland, urban, barren, and other). Forest consists of all forest-related classes in the IGBP classification (IGBP class 1–5). Shrubland includes closed shrublands (IGBP class 6), and open shrublands (IGBP class 7). Savanna class comprises woody savanna (IGBP class 8) and savanna (IGBP class 9). Croplands (IGBP class 12) and cropland/natural vegetation mosaics (IGBP class 14) in IGBP have been combined into the new cropland class. Grassland, urban, and barren classes correspond to the same IGBP classes. The “other” class includes permanent wetlands, snow and ice,

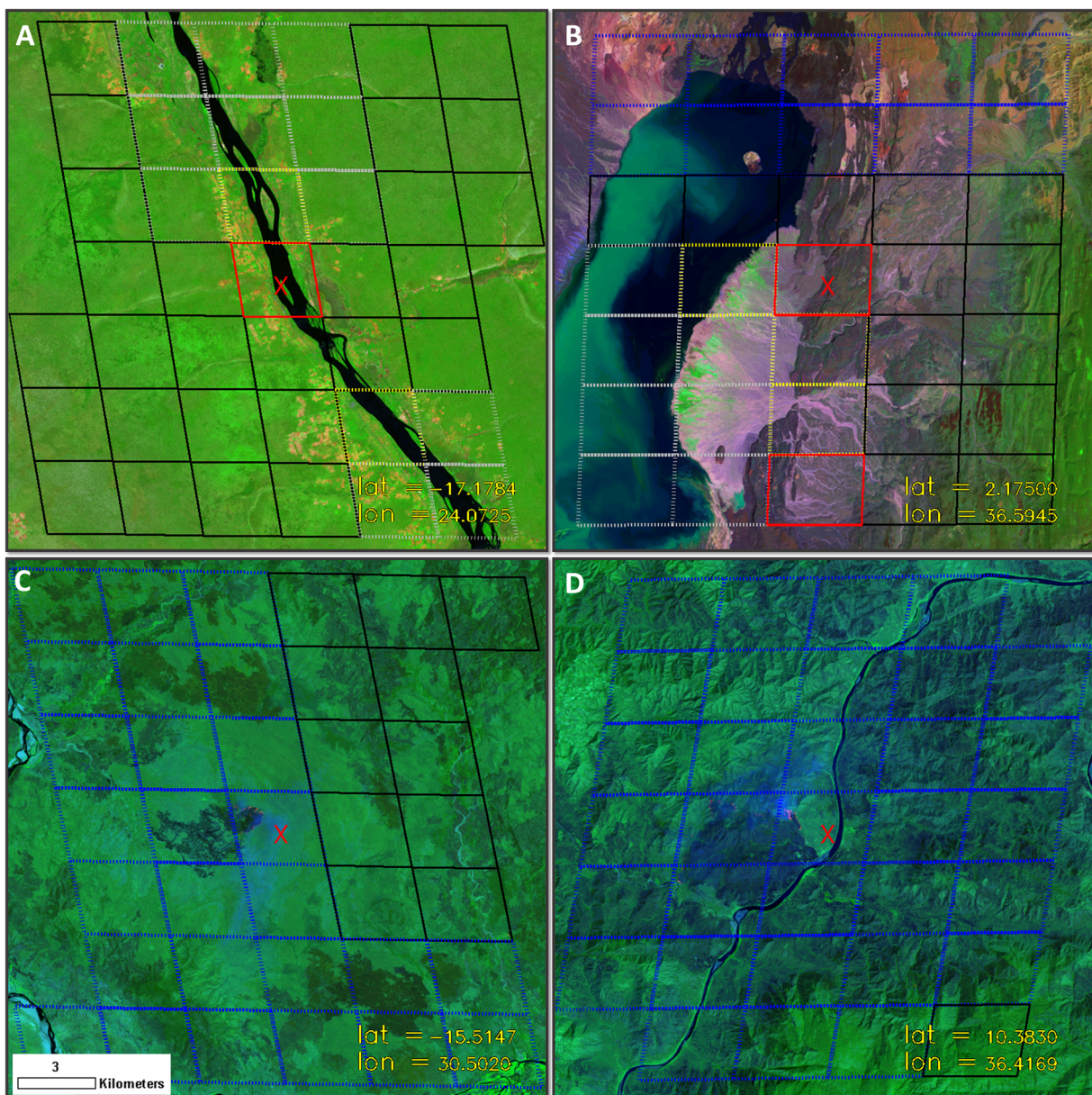


**Fig. 7.** FRP-PIXEL examples of incorrectly masked water bodies causing false alarms or large omissions. Blue squares represent pixels identified as water/invalid ecosystems, white squares represent pixels identified as clouds, red squares represent pixels identified as a fire, and black represent pixels identified as clear land. The latitude and longitude values (bottom right in each panel) describe the approximate coordinate of the center of each pixel marked with a red ‘×’. (For interpretation of the references to colour in this figure legend, the reader is referred to the web version of this article).

water, and unclassified land cover classes. A majority rule was applied to each validation pixel; in those rare instances of a tie, the final land cover class was randomly selected from the tied classes.

### 3. Methods

Our validation methodology builds on previous MODIS Terra Fire and Thermal Anomalies and GOES WF-ABBA product validation efforts (Morisette et al., 2005a, b; Schroeder et al., 2008b). Using near-coincident Landsat-8 OLI imagery, we set out to assess the sub-pixel ABI and SEVIRI fire activity. The ~19,000 OLI 30-m reference images provide a quantitative measure of fire activity within the effective ABI and SEVIRI pixel footprints. Only OLI reference images available within a 5-minute (6-minute) separation of the mid-scan time of ABI (SEVIRI) were used to ensure consistent observation and fire conditions across the respective sensors.

Each ABI or SEVIRI fire pixel was co-located with the 30-m reference OLI data, and summary fire statistics were extracted for each pixel, including fire pixel latitude and longitude, fire pixel mask value (ABI FDC), fire confidence (SEVIRI FRP-PIXEL), reference pixel count, adjacent reference pixel count and the corresponding distance to the fire pixel, fire pixel area, quality information (cloud cover, water, saturation, etc.), percentage tree cover, and majority land cover classification. Including the count of adjacent reference pixels in the analysis helps reduce the number of false alarms as the ABI and SEVIRI footprints are substantially larger than the smaller 30-m OLI pixels. To account for the increase in the footprint area of the ABI and SEVIRI pixels away from the sub-satellite point, a variable circular distance buffer ( $d$ ) was applied to each validation fire pixel, where:

$$d = 1.5 \times \sqrt{\text{fire pixel area}} \quad (1)$$

A true positive was defined in our analyses as an FDC or FRP-PIXEL

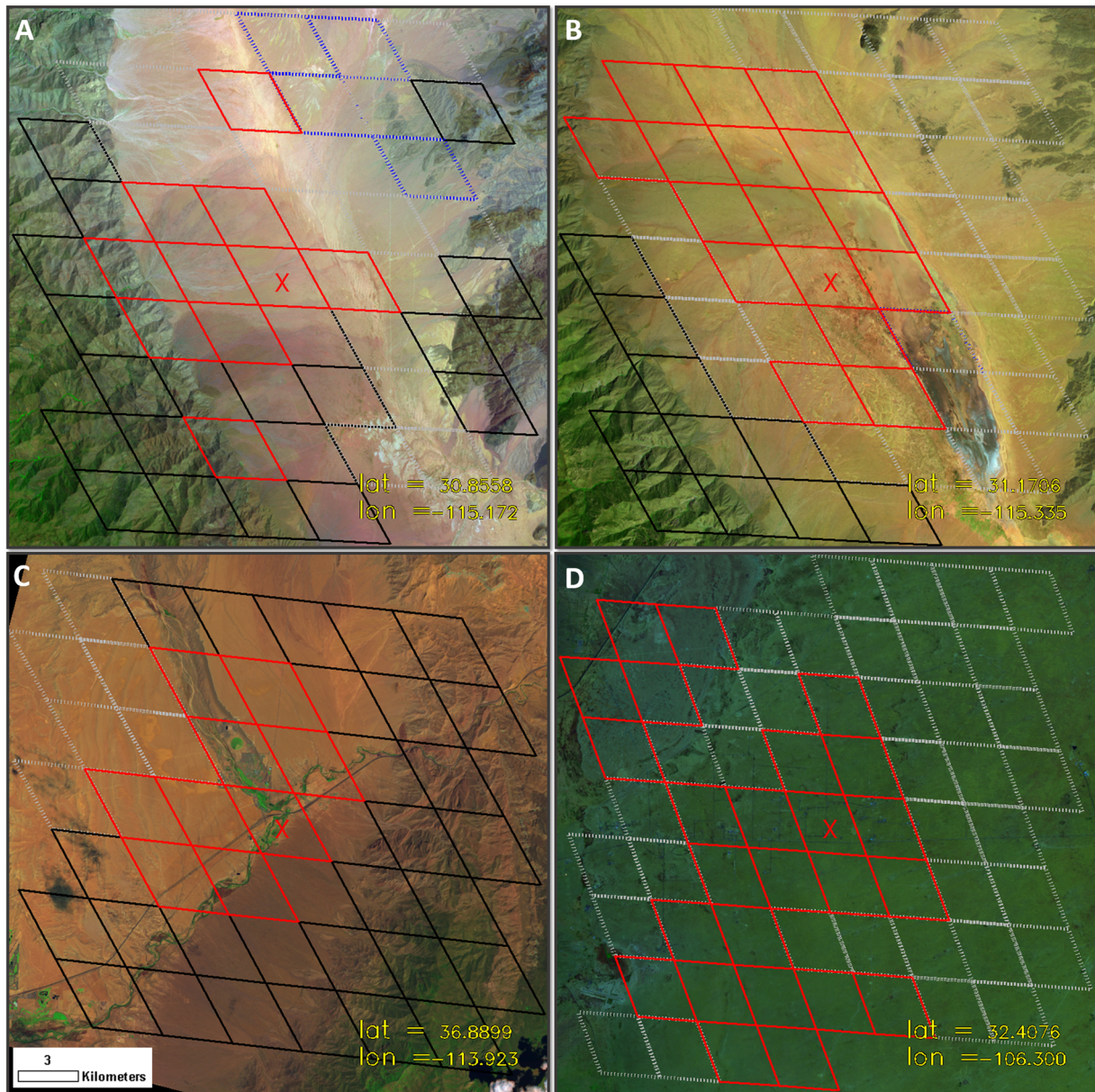


**Fig. 8.** FDC examples of false alarms over sparsely vegetated and bare soil regions. Blue squares represent pixels identified as water/invalid ecosystems, white squares represent pixels identified as clouds, red squares represent pixels identified as a fire, and black represent pixels identified as clear land. The latitude and longitude values (bottom right in each panel) describe the approximate coordinate of the center of each pixel marked with a red '×'. (For interpretation of the references to colour in this figure legend, the reader is referred to the web version of this article).

fire pixel which contained either a reference fire pixel within the effective ABI or SEVIRI pixel bounds or within the distance buffer  $d$ .

#### 4. Results and discussion

Both geostationary active fire products were validated over the respective disk's approximate peak fire season. Our results demonstrate the stark differences between the FDC and the FTA algorithms. In total, 43,113 ABI and 300,945 SEVIRI pixels were sampled including fire/non-fire/land/water/clouds. As expected, the majority of correctly detected validation fire pixels were concentrated near the sub-satellite point as opposed to the regions near the disk edges where the geostationary pixel areas grew to more than 8 times larger (Fig. 2).

#### 4.1. Detection rate

In order to facilitate the inter-comparison between the FDC and FRP-PIXEL detection rates, individual OLI reference fire pixels were assumed to represent a constant 900-m<sup>2</sup> active fire area so that the corresponding fire fractional areas could be calculated based on ABI's and SEVIRI's effective pixel footprints. This crude assumption was exclusively meant to allow a detection rate evaluation and is not to be confused with actual fire area mapped. In fact, sub-pixel fire activity likely dominates even the comparatively high-resolution OLI reference pixels, therefore the approximation used here should be seen as an upper limit estimate. Consequently, the fractional areas we report are likely larger than the actual areas.

Plotting the detection rate as a function of fractional area helps normalize these results allowing for a general comparison between the active fire products (Fig. 3). The irregular detection rate curves are an

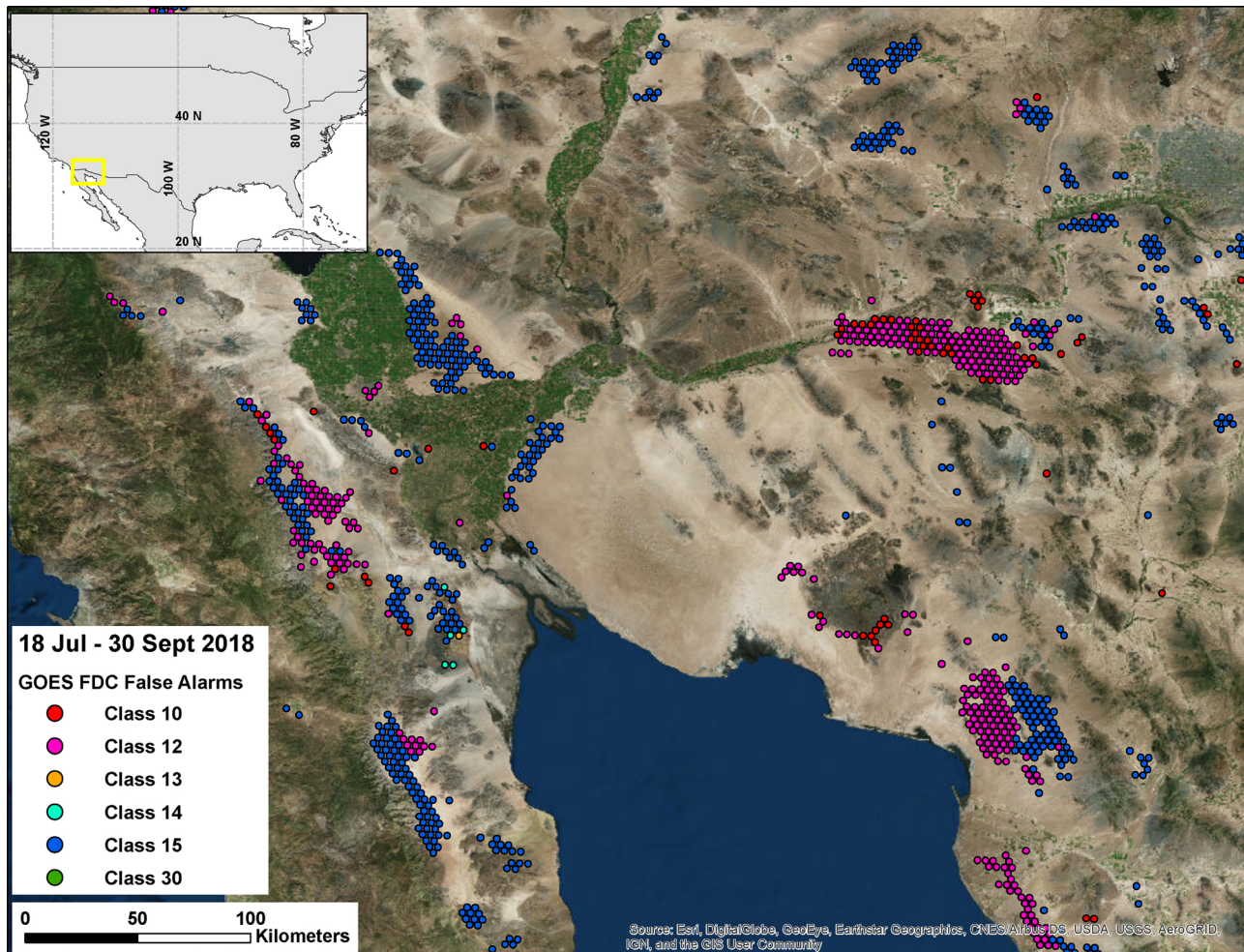


**Fig. 9.** Large swaths of FDC daytime false alarms in regions of homogenous bright desert soil regions in northern Mexico, southern Arizona and Western Texas.

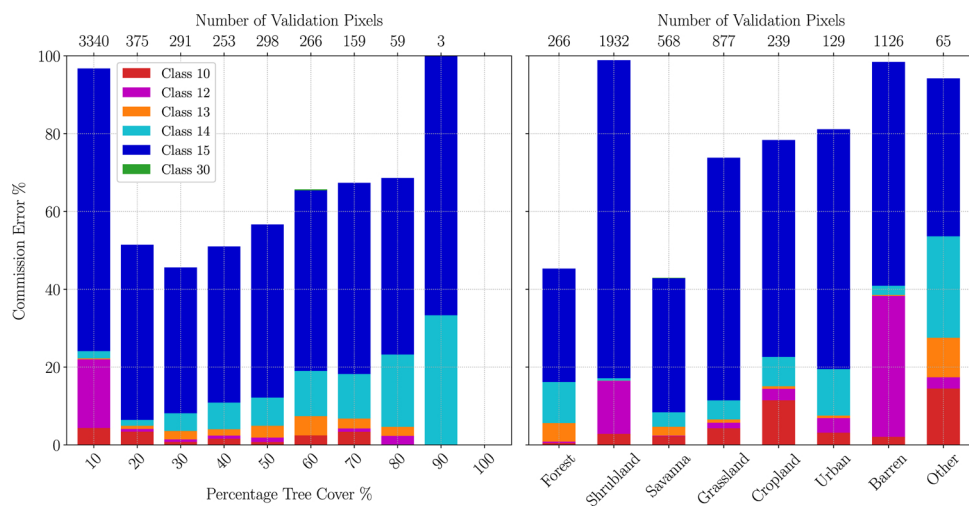


**Fig. 10.** FDC commission error as a function of percentage tree cover (left) and majority MODIS land cover (right).

artifact of the small sample sizes within each fractional area bin. Although active fires much smaller than the pixel footprint are able to be detected, e.g., 0.01-ha fire within a 1-km MODIS pixel (Giglio et al., 2003), the large number of missed small fires is unsurprising since the geostationary sensor spatial footprints vary considerably; a reference fire of 0.1% fractional area of an ABI pixel near the edge of the disk, for example, would require a fire to span several hundred 900-m<sup>2</sup> reference

fire pixels.

#### 4.2. Commission and omission errors

Of the 43,113 ABI validation pixels, 36,384 pixels (84%) were labeled as a non-fire pixel yet were flagged as containing coincident reference fire activity within 5-minutes of the overpass and therefore

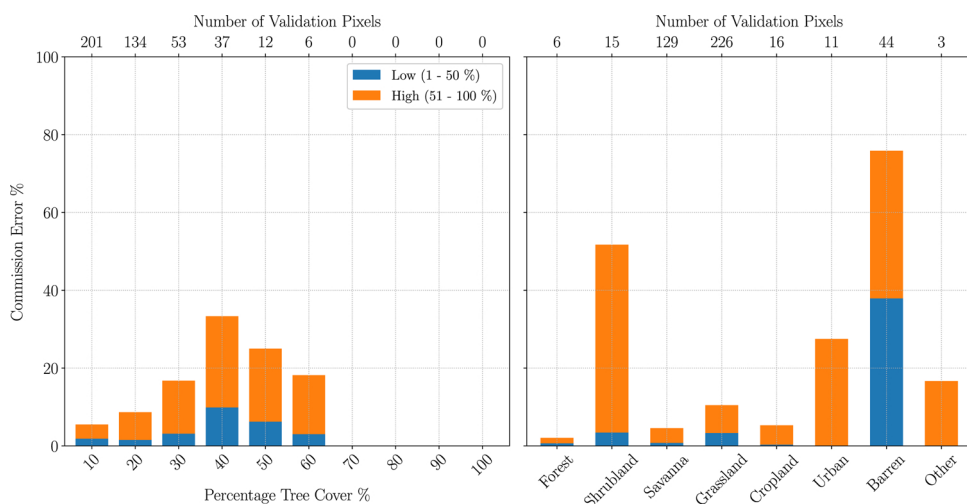


**Fig. 11.** FRP-PIXEL commission error as a function of percentage tree cover (left) and majority MODIS land cover (right). The low/high confidence values were split at the 50% confidence value.

characterized as an omission error. Of the 300,945 SEVIRI validation pixels, 295,227 pixels (98%) were flagged as non-fire yet contained coincident reference fire activity within 6-minutes of the overpass. As noted above, the restrictive temporal window was enforced to reduce the impact of changes in fire activity between the time of the Landsat-8 overpass and the respective GOES-16 ABI or MSG SEVIRI scan. Furthermore, 57,201 (~20%) of the SEVIRI omission pixels are directly related to cloud and cloud-edge pixels which are masked out within the FTA algorithm (see section 2.2.1 for algorithm details).

Analysis of the underlying reference fire activity in the omitted FDC and FRP-PIXEL fire pixels found that the vast majority were located in areas with low percentage tree cover (on average 24% for FDC and 12% for FRP-PIXEL) and within pixels over double the original spatial resolution with median areas of 6-km<sup>2</sup> (ABI) and 13-km<sup>2</sup> (SEVIRI). Further analysis of FDC and FRP-PIXEL omitted fire pixels also found that over 70% contained 5 or fewer OLI reference fire pixels and ~90% contained 15 or fewer reference OLI fire pixels. Based on the fractional area detection rates (Fig. 3), it is unsurprising that the majority of these omissions occurred in ABI/SEVIRI pixels with a small number of OLI fire pixels.

Analysis of the remaining fire pixels (6729 for FDC and 5718 for FRP-PIXEL) found that, overall, the FDC product contains a lower proportion of true positives, with only 22% of fire pixels flagged correctly (including all fire pixel classes), compared to 92% of the FRP-PIXEL data (including all confidence values). The FDC product is created with pre-defined fire classes (see section 2.1), therefore, subdividing the commission error by ABI class further highlights the large proportion of false alarms, especially in the low probability class 15 (Fig. 4). Approximately 58% of the 6729 FDC fire pixels were incorrectly identified and labeled as a class 15 fire. Unlike the FDC product, the FRP-PIXEL product is created with a fire confidence (0–100%) value assigned to each fire pixel. Multiple high/low confidence thresholds (split at 50%, 60%, 77% (mean), and 78% (median)) were applied to the validation dataset and it was found that the commission error was not very sensitive to the high/low threshold cutoff. Therefore, we chose to illustrate the high/low confidence cutoff at 50% (see Fig. 4).

The smaller proportion of low confidence values in the FRP-PIXEL product is a striking difference when compared to the FDC product. The number of incorrectly identified fire pixels ranged between 119 and 350 pixels depending on where the division between low and high confidence fires was established. Using all confidence values, this number increased to 457 misclassified pixels, which is substantially lower than the 5214 false alarms (all classes) in the FDC product. The

overall smaller number of commission errors in the FRP-PIXEL product is unsurprising since the algorithm is seemingly more restrictive than the FDC product. FDC classes 31–35 were absent in the sample analyzed.

#### 4.2.1. Commission and omission errors: land cover analysis

While visually inspecting the validation data output during the quality control phase, several patterns emerged, particularly with respect to the FDC product and these were further confirmed through analysis with the VCF and MODIS land cover products (see section 2.4 for details). Both products were impacted by either clouds/cloud-shadows (FDC) or by an overzealous cloud mask (FRP-PIXEL) (Fig. 5).

Based on the cloud persistence (clouds were extracted from each product's QA files) over the two time periods, it is clear during the FRP-PIXEL product sampling period there were large regions with highly persistent clouds (Fig. 6). With the very restrictive mapping requirements in the FTA algorithm, it is clear a large number of fires are likely to be missed in the FRP-PIXEL product. A visual comparison with cloud cover extracted from the daily Level 3 MODIS Atmosphere Daily Global Product (MOD08/MYD08; 1° resolution) using the NASA Giovanni software (<https://giovanni.gsfc.nasa.gov/giovanni/>) found similar overall patterns of cloud persistence; however, comparisons with the reference Landsat-8 scenes (e.g. Fig. 5c and d) seems to indicate the FTA algorithm's cloud mask may be detrimentally impacting the FRP-PIXEL fire product through over mapping cloud cover.

Urban areas also caused a number of false detections for both products. Although some confusion with urban areas also occur in the FRP-PIXEL product, the predominant issue causing a larger number of omissions was found to be related to the cloud and water masks (Fig. 7).

The largest cause of false alarms in the FDC product occurred over sparsely vegetated and bare soil regions (Figs. 8 and 9). These large swaths of misclassified fire pixels were not evident in the FRP-PIXEL product. Although the landscape and fire types differ over the two geostationary spatial disks, it is believed that this issue is a direct result of the differences in the underlying algorithms.

The frequent misclassification of fire pixels over sparsely vegetated and bare soil regions is also evident when analyzing the commission error as a function of the percentage tree cover and majority MODIS land cover (Fig. 10). More than 60% of the false alarms occur within pixels with an average tree cover percentage of less than 10% and within shrubland and barren land cover classes.

In general, the FRP-PIXEL output found that the highest rate of false alarms occurred within areas of more than 40% tree cover (Fig. 11). Similarly, false alarm rates were also higher in the barren and

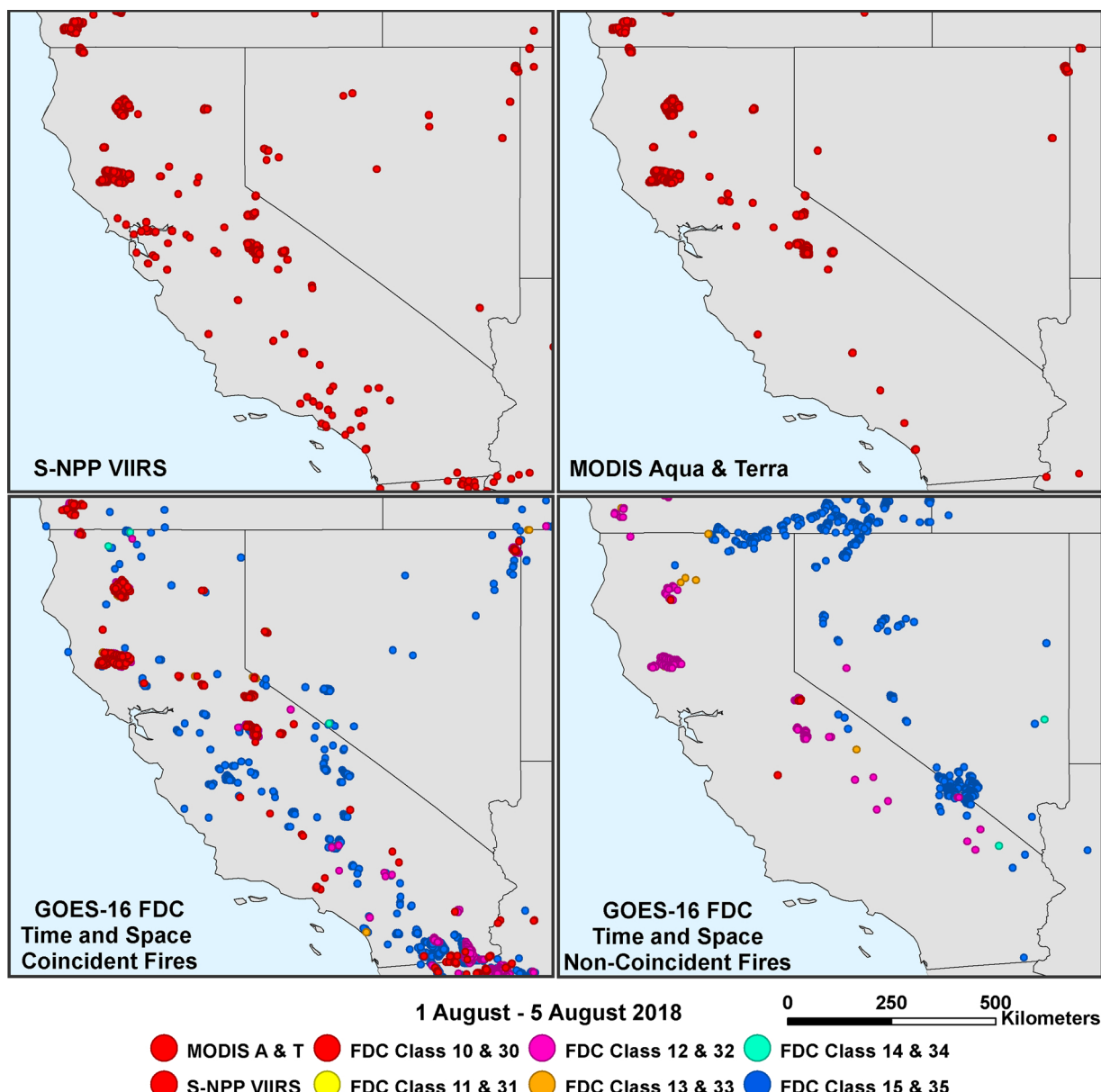


**Fig. 12.** Visual comparison between S-NPP VIIRS (top left), MODIS Aqua and Terra (top right) and coincident (bottom left) in both time ( $\leq 1$ -h separation) and space ( $\leq 1^\circ$ ) and non-coincident (bottom right) FDC active fires between 1 August and 5 August 2018 over California and Nevada. For clarity the active fire detections for all products have been displayed as fixed-size points at the central latitude and longitude of each fire pixel and does not represent actual pixel or fire sizes. (For interpretation of the references to colour in this figure legend, the reader is referred to the web version of this article).

shrubland land cover classes.

#### 4.3. Comparison with MODIS and VIIRS active fire products

Comparison of the FDC and FRP-PIXEL active fire products with the Suomi-National Polar-orbiting Partnership (S-NPP) Visible Infrared Imaging Radiometer Suite (VIIRS) 375-m (Schroeder et al., 2014) and the MODIS Aqua and Terra (500-m) active fire products (Giglio et al., 2016) further highlight the differences between these two geostationary fire products (Figs. 12 and 13, respectively). Here maps were created for a period of 5 days per time period (1 January – 5 January 2018 for FRP-PIXEL and 1 August – 5 August 2018 for FDC) highlighting the FDC and FRP-PIXEL detections that were within a 1-h temporal separation and within  $1^\circ$  spatial separation from a MODIS or a VIIRS active fire pixel. These time- and space-coincident and non-coincident fires were plotted and compared against the polar-orbiting active fire products. Noticeably, a larger portion of FRP-PIXEL fire pixels were outside of

these spatial and temporal windows than the FDC ones. These FRP-PIXEL results highlight one of the advantages of geostationary active fire datasets. The higher temporal resolution leads to a higher likelihood of detecting additional fires than their polar-orbiting counterparts. However, as highlighted throughout this manuscript, the FDC active fire product suffers from a large number of false alarms and these are evident along the border of California and Nevada (blue dots Fig. 12, bottom right) where large swaths of uncorroborated fire pixels are mapped over bright soil regions.

#### 4.4. Harmonized multi-sensor global geostationary active fire dataset

This validation study is part of a larger project focused on developing a harmonized multi-sensor global geostationary active fire dataset. These validation results will be used to guide the data harmonization procedure through collaboration with the active fire algorithm developers to identify targeted algorithm improvements. More broadly,

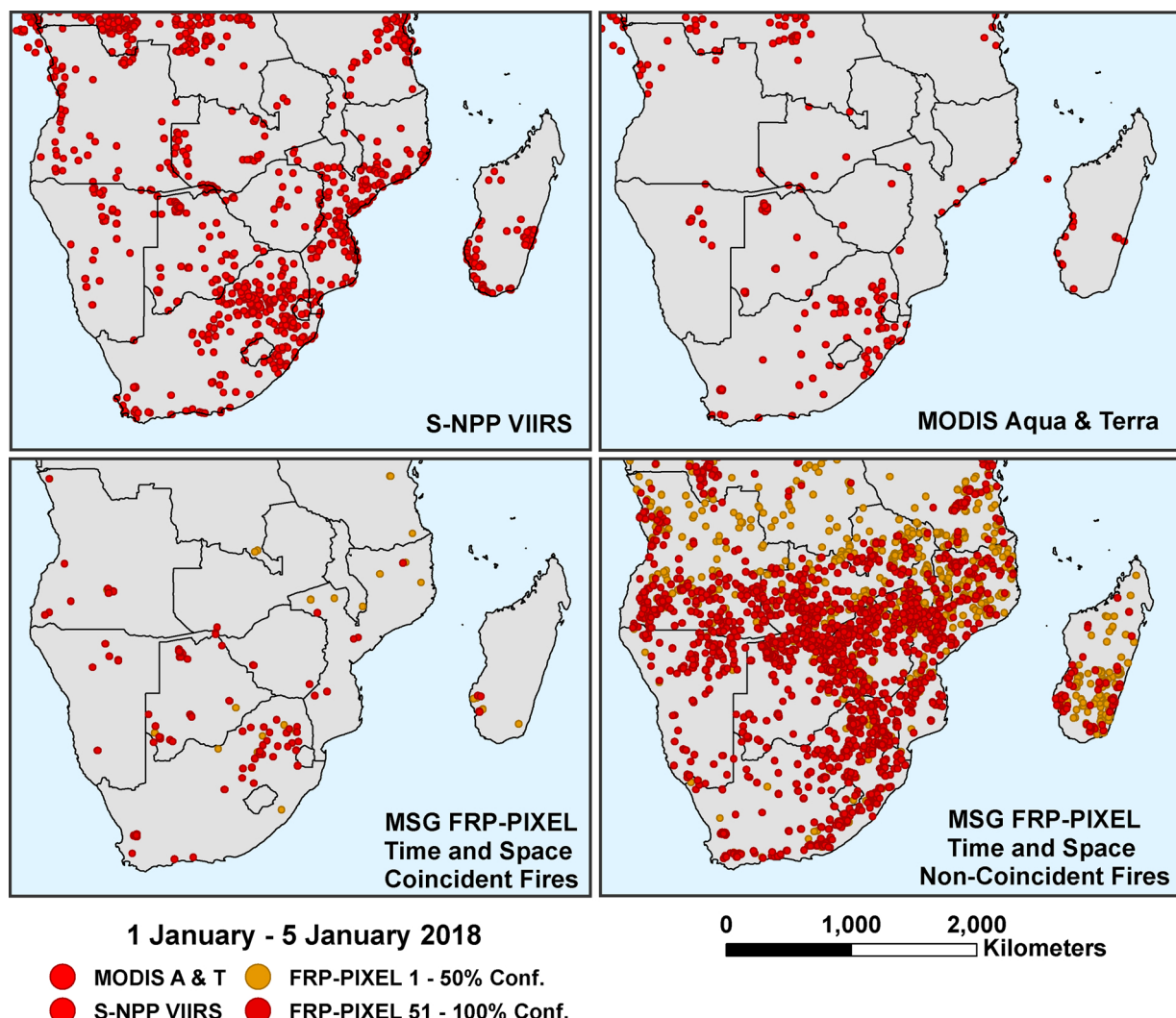


**Fig. 13.** Comparison between S-NPP VIIRS (top left), MODIS Aqua and Terra (top right) and coincident (bottom left) and non-coincident (bottom right) FRP-PIXEL fire products between 1 January and 5 January 2018 over the southern portion of Africa. For clarity the active fire detections for all products have been displayed as fixed-size points at the central latitude and longitude of each fire grid pixel and does not represent actual pixel or fire sizes. (For interpretation of the references to colour in this figure legend, the reader is referred to the web version of this article).

our validation results also highlight the importance of understanding the differences, strengths, and limitations of these data, particularly when they are used in combination. By validating both FDC and FRP-PIXEL products with the same validation protocol, we were able to further highlight the significant differences in the two geostationary active fire data sets. For example, while each product contains omission and commission errors, we found a much greater likelihood of misclassified fire pixels in the FDC product than for the FRP-PIXEL product. Although there are differing fire sizes and regimes within the two hemispheres, the large swaths of misclassified FDC fire pixels (e.g. Fig. 9), particularly within the lower probability classes, are likely a by-product of the algorithm heritage which on the one hand under-utilizes the spectral and temporal information available with ABI, and on the other uses several ancillary data layers with no apparent gain in performance. These results illustrate the importance of algorithm tuning to sensor-specific characteristics, and moreover the need to further explore active fire detection methodologies that can fully utilize the greatly improved temporal information available with the new generation of Earth-observing geostationary sensors. Based on the omission and commission error results (Fig. 4), the SEVIRI FTA algorithm's thresholds are seemingly more restrictive than the ABI FDC algorithm; however, we believe the decision to limit fire detections within partly

cloudy pixels is detrimentally impacting the FRP-PIXEL product. In addition, the greater proportion of FRP-PIXEL omission pixels (98%) as compared to FDC (84%) helps partially explain why the former had comparatively lower commission errors.

Harmonizing these two active fire products – one with a conservative detection algorithm and one which is beset with large swaths of false fire pixels – will be challenging but these validation results are the first important step into identifying the methodological framework for the larger harmonization study. Our results may also be taken as a cautionary note for those looking to combine active fire data from different sensors.

## 5. Conclusion

Using Landsat-8 OLI as reference fire data, we validated active fire products derived from GOES-16 ABI and the MSG SEVIRI for two periods in 2017 and 2018. The results of our validation of the FDC and the FRP-PIXEL products highlight some important issues that need to be addressed with targeted improvements to both algorithms. The current FDC algorithm continues to evolve therefore it is crucial for users to follow the algorithm changes outlined in the ATBD and any future validation results. Future changes to either products must be

transferred to archived data, including provisions for full data reprocessing and long-term quality monitoring.

Specifically, our results draw attention to the dichotomy of these two seemingly complementary geostationary active fire products. Firstly, the elevated sensitivity of the FDC algorithm (88% commission error) compared to FTA (8% commission error) was demonstrated throughout this paper with multiple examples of misclassified FDC fire pixels, especially within desert regions (e.g., Fig. 8). Secondly, the restrictiveness of the FRP-PIXEL product (98% omission error, 295,277 pixels out of 300,945 pixels) compared to FDC (84% omission error; 36,384 pixels out of 43,113 pixels) was also demonstrated. The complete dismissal of partially cloudy or optically thin cloudy pixels within the FTA algorithm is one of the causes of the high omission error (e.g., Fig. 5).

This study revealed the need for further investments in the development of robust active fire detection algorithms for geostationary Earth-observing satellites. Historically, geostationary satellite fire detection algorithms have been relinquished to a secondary role in the fire community, with fewer applications and lesser user demand due – primarily – to the lower overall spatial quality of the information. The lack of comprehensive algorithm documentation and validation studies, properly maintained archives (including data reprocessing for long-term consistency and ease of access), and adequate geographical coverage created additional limitations for the adoption of those data by the fire management and science communities. Currently, two main systems provide near-complete coverage of most fire-prone regions globally, namely NOAA's GOES-R ABI (two satellites positioned at 75.2° and 137.2°W, along with its sister instrument AHI onboard Japan's Himawari-8/9 140.7°E orbit) and EUMETSAT's MSG (two satellites positioned at 0° and 41.5°E). With only two distinct sensing systems providing such broad spatial coverage, the investment in algorithm development, tuning, and implementation could be greatly optimized while at the same time favoring improved geostationary satellite fire data consistency across regions. In order to achieve that goal, a concerted effort by the satellite fire community will be needed to develop, test, and validate algorithms and end products meeting basic user requirements. Until then, data filtering (e.g., minimizing false alarms) and harmonization procedures will have to be implemented to improve overall data quality and interoperability when using different geostationary data sets.

## Declaration of Competing Interest

None

## Acknowledgments

This work was supported by NASA Applied Sciences Program grant 80NSSC18K0833 and by the NOAA GOES-R program.

## References

- Aminou, D.M.A., 2002. MSG's SEVIRI instrument. *ESA Bull.-Eur. Space* 111, 15–17.
- Bowman, D., Balch, J.K., Artaxo, P., Bond, W.J., Carlson, J.M., Cochrane, M.A., D'Antonio, C.M., DeFries, R.S., Doyle, J.C., Harrison, S.P., Johnston, F.H., Keeley, J.E., Krawchuk, M.A., Kull, C.A., Marston, J.B., Moritz, M.A., Prentice, I.C., Roos, C.I., Scott, A.C., Swetnam, T.W., van der Werf, G.R., Pyne, S.J., 2009. Fire in the earth system. *Science* 324, 481–484. <https://doi.org/10.1126/science.1163886>.
- Cochrane, M.A., 2003. Fire science for rainforests. *Nature* 421, 913–919.
- Derrien, M., Le Gleau, H., 2005. MSG/SEVIRI cloud mask and type from SAFNWC. *Int. J. Remote Sens.* 26, 4707–4732. <https://doi.org/10.1080/01431160500166128>.
- DiMiceli, C.M., Carroll, M.L., Sohlberg, R.A., Huang, C., Hansen, M.C., Townshend, J.R.G., 2011. Annual Global Automated MODIS Vegetation Continuous Fields (MOD44B) at 250 M Spatial Resolution. University of Maryland, College Park. <http://glcf.umd.edu/data/vcf/>.
- Dozier, J., 1981. A method for satellite identification of surface temperature fields of subpixel resolution. *Remote Sens. Environ.* 11, 221–229. [https://doi.org/10.1016/0034-4257\(81\)90021-3](https://doi.org/10.1016/0034-4257(81)90021-3).
- Friedl, M., Sulla-Menashe, D., 2019. MCD12Q1 MODIS/Terra + Aqua Land Cover Type Yearly L3 Global 500m SIN Grid V006. 2019. NASA EOSDIS Land Processes DAAC.
- Giglio, L., Csizsar, I., Restás, Á., Morisette, J.T., Schroeder, W., Morton, D., Justice, C.O., 2008. Active fire detection and characterization with the advanced spaceborne thermal emission and reflection radiometer (ASTER). *Remote Sens. Environ.* 112, 3055–3063.
- Giglio, L., Descloitre, J., Justice, C.O., Kaufman, Y.J., 2003. An enhanced contextual fire detection algorithm for MODIS. *Remote Sens. Environ.* 87, 273–282. [https://doi.org/10.1016/S0034-4257\(03\)00184-6](https://doi.org/10.1016/S0034-4257(03)00184-6).
- Giglio, L., Schroeder, W., Justice, C.O., 2016. The collection 6 MODIS active fire detection algorithm and fire products. *Remote Sens. Environ.* 178, 31–41. <https://doi.org/10.1016/j.rse.2016.02.054>.
- Govaerts, Y., Wooster, M., Roberts, G., Freeborn, P., Xu, W., He, J., Lattanzio, A., 2016. Algorithm Theoretical Basis Document for MSG SEVIRI Fire Radiative Power (FRP) Characterisation (p. 33). EUMETSAT. <https://landsat.ipma.pt/GetDocument.do?id=682>.
- Hansen, M.C., DeFries, R.S., Townshend, J.R.G., Marufu, L., Sohlberg, R., 2002. Development of a MODIS tree cover validation data set for Western Province, Zambia. *Remote Sens. Environ.* 83, 320.
- Hyer, E.J., Reid, J.S., 2009. Baseline uncertainties in biomass burning emission models resulting from spatial error in satellite active fire location data. *Geophys. Res. Lett.* 36. <https://doi.org/10.1029/2008gl036767>.
- Justice, C.O., Giglio, L., Korontzi, S., Owens, J., Morisette, J.T., Roy, D., Descloitre, J., Alleaume, S., Petitclain, F., Kaufman, Y., 2002. The MODIS fire products. *Remote Sens. Environ.* 83, 244.
- Koltunov, A., Ustin, S.L., Prins, E.M., 2012. On timeliness and accuracy of wildfire detection by the GOES WF-ABBA algorithm over California during the 2006 fire season. *Remote Sens. Environ.* 127, 194–209. <https://doi.org/10.1016/j.rse.2012.09.001>.
- Lohman, D.J., Bickford, D., Sodhi, N.S., 2007. The burning issue. *Science* 316, 376. <https://doi.org/10.1126/science.1140278>.
- MeteoFrance, 2007. Algorithm Theoretical Basis Document for Cloud Products. Technical Report. MeteoFrance.
- Morisette, J.T., Giglio, L., Csizsar, I., Justice, C.O., 2005a. Validation of the MODIS active fire product over Southern Africa with ASTER data. *Int. J. Remote Sens.* 26, 4239–4264. <https://doi.org/10.1080/01431160500113526>.
- Morisette, J.T., Giglio, L., Csizsar, I., Setzer, A., Schroeder, W., Morton, D., Justice, C.O., 2005b. Validation of MODIS active fire detection products derived from two algorithms. *Earth Interact.* 9, 1–25. <https://doi.org/10.1175/EI141.1>.
- Picotte, J.J., Peterson, B., Meier, G., Howard, S.M., 2016. 1984–2010 trends in fire burn severity and area for the conterminous US. *Int. J. Wildland Fire* 25, 413–420. <https://doi.org/10.1071/WF15039>.
- Prins, E.M., Feltz, J.M., Menzel, W.P., Ward, D.E., 1998. An overview of GOES-8 diurnal fire and smoke results for SCAR-B and 1995 fire season in South America. *J. Geophys. Res. Atmos.* 103, 31821–31835. <https://doi.org/10.1029/98JD01720>.
- Prins, E.M., Menzel, W.P., 1992. Geostationary satellite detection of bio mass burning in South America. *Int. J. Remote Sens.* 13, 2783–2799. <https://doi.org/10.1080/01431169208904081>.
- Prins, E.M., Menzel, W.P., 1994. Trends in South American biomass burning detected with the GOES visible infrared spin scan radiometer atmospheric sounder from 1983 to 1991. *J. Geophys. Res. Atmos.* 99, 16719–16735. <https://doi.org/10.1029/94jd01208>.
- Roberts, G., Wooster, M.J., Perry, G.L.W., Drake, N., Rebelo, L.M., Dipotso, F., 2005. Retrieval of biomass combustion rates and totals from fire radiative power observations: Application to southern Africa using geostationary SEVIRI imagery. *J. Geophys. Res. Atmos.* 110. <https://doi.org/10.1029/2005JD006018>.
- Schmidt, C., Hoffman, J., Prins, E., Lindstrom, S., 2012. GOES-R Advanced Baseline Imager (ABI) Algorithm Theoretical Basis Document For Fire/ Hot Spot Characterization (p. 97). <https://www.star.nesdis.noaa.gov/goesr/docs/ATBD/Fire.pdf>.
- Schroeder, W., Csizsar, I., Morisette, J., 2008a. Quantifying the impact of cloud obscuration on remote sensing of active fires in the Brazilian Amazon. *Remote Sens. Environ.* 112, 456–470. <https://doi.org/10.1016/j.rse.2007.05.004>.
- Schroeder, W., Oliva, P., Giglio, L., Csizsar, I.A., 2014. The New VIIRS 375 m active fire detection data product: algorithm description and initial assessment. *Remote Sens. Environ.* 143, 85–96. <https://doi.org/10.1016/j.rse.2013.12.008>.
- Schroeder, W., Oliva, P., Giglio, L., Quayle, B., Lorenz, E., Morelli, F., 2016. Active fire detection using Landsat-8/OLI data. *Remote Sens. Environ.* 185, 210–220. <https://doi.org/10.1016/j.rse.2015.08.032>.
- Schroeder, W., Prins, E., Giglio, L., Csizsar, I., Schmidt, C., Morisette, J., Morton, D., 2008b. Validation of GOES and MODIS active fire detection products using ASTER and ETM + data. *Remote Sens. Environ.* 112, 2711–2726. <https://doi.org/10.1016/j.rse.2008.01.005>.
- Schroeder, W., Ruminski, M., Csizsar, I., Giglio, L., Prins, E., Schmidt, C., Morisette, J., 2008c. Validation analyses of an operational fire monitoring product: the Hazard Mapping System. *Int. J. Remote Sens.* 29, 6059–6066. <https://doi.org/10.1080/01431160802235845>.
- Trigo, I.F., Dacamara, C.C., Viterbo, P., Roujeau, J.-L., Olesen, F., Barroso, C., Camacho-de-Coca, F., Carrer, D., Freitas, S.C., García-Haro, J., Geiger, B., Gellens-Meulenberghs, F., Ghilain, N., Meliá, J., Pessanha, L., Siljamo, N., Arboleda, A., 2011. The satellite application facility for land surface analysis. *Int. J. Remote Sens.* 32, 2725–2744. <https://doi.org/10.1080/01431161003743199>.
- Wooster, M.J., Roberts, G., Freeborn, P.H., Xu, W., Govaerts, Y., Beeby, R., He, J., Lattanzio, A., Fisher, D., Mullen, R., 2015. LSA SAF Meteosat FRP products – part 1: algorithms, product contents, and analysis. *Atmos. Chem. Phys.* 15, 13217–13239. <https://doi.org/10.5194/acp-15-13217-2015>.
- Wooster, M.J., Zhukov, B., Oertel, D., 2003. Fire radiative energy for quantitative study of biomass burning: derivation from the BIRD experimental satellite and comparison to MODIS fire products. *Remote Sens. Environ.* 86, 83–107. [https://doi.org/10.1016/S0034-4257\(03\)00070-1](https://doi.org/10.1016/S0034-4257(03)00070-1).
- Xu, W., Wooster, M.J., Roberts, G., Freeborn, P., 2010. New GOES imager algorithms for cloud and active fire detection and fire radiative power assessment across North, South and Central America. *Remote Sens. Environ.* 114, 1876–1895. <https://doi.org/10.1016/j.rse.2010.03.012>.